MUSE observations that affirm the path to detonation of a Type Ia supernova in a supernova remnant

Priyam Das[1,2*†], Ivo R. Seitenzahl[2*†], Ashley J. Ruiter[1,2,3,4], Friedrich K. Röpke[2,5,6], Rüdiger Pakmor[7], Frédéric P. A. Vogt[8], Christine E. Collins[9,10], Parviz Ghavamian[11], Stuart A. Sim[12], Brian J. Williams[13], Stefan Taubenberger[14,15], J. Martin Laming[16], Janette Suherli[17], Ralph Sutherland[18], Nicolas R. Segovia[1]

[1]School of Science, University of New South Wales, Australian Defence Force Academy, Northcott Drive, Canberra, 2600, ACT, Australia.

[2]Heidelberger Institut für Theoretische Studien, Schloss-Wolfsbrunnenweg 35, Heidelberg, 69118, Germany.

[3]OzGrav: The ARC Centre of Excellence for Gravitational Wave Discovery, Hawthorn, VIC 3122, Australia.

[4]ARC Centre of Excellence for All-Sky Astrophysics in 3 Dimensions (ASTRO-3D).

[5]Zentrum für Astronomie der Universität Heidelberg, Institut für Theoretische Astrophysik, Philosophenweg 12, Heidelberg, 69120, Germany.

[6]Zentrum für Astronomie der Universität Heidelberg, Astronomisches Recheninstitut, Mönchhofstraße 12 – 14, Heidelberg, 69120, Germany.

[7]Max-Planck-Institut für Astrophysik, Karl-Schwarzschild-Str. 1, Garching, 85748, Germany.

[8]Federal Office of Meteorology and Climatology – MeteoSwiss, Chemin de l'Aérologie 1, Payerne, 1530, Switzerland.

[9]School of Physics, Trinity College Dublin, The University of Dublin, Dublin 2, Dublin, Ireland.

[9]GSI Helmholtzzentrum für Schwerionenforschung, Planckstraße 1, Darmstadt, 64291, Germany.

[11]Department of Physics Astronomy and Geosciences, Towson University, 8000 York Road, Towson, MD, 21252,USA.

[12]School of Mathematics and Physics, Queen's University Belfast, University Road, Belfast BT7 INN, UK.

[13]X-ray Astrophysics Laboratory NASA/GSFC, MD, Greenbelt, 20771, USA.
[14]Max-Planck-Institute for Astrophysics, Karl-Schwarzschild-Str. 1, Garching, 85741, Germany.
[15]TUM Department of Phyiscs, Technical University Munich, James-Franck-Str. 1., Garching, 85741, Germany.
[16]Space Science Division, Code 7684, Naval Research Laboratory, Washington, DC 20375, USA.
[17]Department of Physics and Astronomy, University of Manitoba, R3T 2N2, Winnipeg, Manitoba, Canada.
[18]Research School of Astronomy and Astrophysics, Australian National University,Weston Creek, ACT, Australia.

*Corresponding author(s). E-mail(s): priyam.das@unsw.edu.au; ivoseitenzahl@gmail.com;
†These authors contributed equally to this work.

Type Ia supernovae play a fundamental role as cosmological probes of dark energy and produce more than half of the iron in our Galaxy [1]. Despite their central importance, a comprehensive understanding of their progenitor systems is still lacking [2]. ***In addition, the triggering mechanism of a thermonuclear explosion*** **in a white dwarf star is** ***still*** **a long-standing fundamental problem. A persistent paradigm [3–5] has been that a white dwarf in a close binary star system can collect mass from the companion star until it approaches the Chandrasekhar mass limit (**$\sim 1.4\ \mathrm{M}_{\odot}$**), resulting in runaway nuclear burning. However, modern simulations and observations disfavour this** ***as the main*** **scenario, and** ***instead*** **favour explosions of less massive white dwarfs producing Type Ia supernovae [6–10].** ***Despite this recent paradigm shift, there is a substantial lack of direct observational evidence in support of either particular explosion pathway leading to a Type Ia explosion, as the respective progenitors are observationally elusive.*** **Our deep observations with the Multi Unit Spectroscopic Explorer (MUSE) of the young supernova remnant SNR 0509-67.5 reveal for the first time** ***in the reverse shocked ejecta a*** **double-shell calcium structure and a single shell of sulphur.** ***This morphology is consistent with the predictions of*** **hydrodynamical double-detonation simulations of sub-Chandrasekhar-mass white dwarf explosions. Our observations** ***provide the first substantial evidence from the supernova remnant phase that*** **sub-Chandrasekhar mass explosions through the double-detonation mechanism do occur in nature.**

1 Main

The question of how a thermonuclear explosion initiates in an inert object like a white dwarf star is an essential and long-standing problem in stellar astrophysics [11]. In a white dwarf consisting of carbon and oxygen and approaching the Chandrasekhar mass, the increasing central density inevitably triggers nuclear burning. The **almost constant** explosion mass that the Chandrasekhar-mass explosion model provides was a popular explanation for the homogeneity initially attributed to Type Ia supernovae [12]. However, the recent wealth of data challenges the notion of homogeneity [13], and a fixed mass seems even problematic for reproducing the width–luminosity relation [14], which is vital for calibrating Type Ia supernovae as cosmological distance indicators. The width–luminosity relation is more naturally explained by a variable **white dwarf** mass below the Chandrasekhar-mass limit as the primary parameter [15, 16]. Moreover, the ability to grow white dwarfs to the Chandrasekhar mass restricts the parameters of the progenitor binary system to a narrow range, so that the observed rate of Type Ia supernovae is hard to reconcile with the expected number of systems consistent with the Chandrasekhar-mass explosion **scenario** [17, 18]. This calls for alternative scenarios involving explosions of carbon-oxygen white dwarf stars well below the Chandrasekhar-mass limit and raises the fundamental problem of how to ignite a thermonuclear explosion in an inert sub-Chandrasekhar mass white dwarf.

A head-on collision of two white dwarfs may seem promising as a pathway for producing sub-Chandrasekhar mass exploding white dwarfs [19], however, this scenario is not favoured because the predicted occurrence rates are too low [20]. The currently most promising scenario for exploding sub-Chandrasekhar mass white dwarfs is a double-detonation: A carbon-oxygen white dwarf collects helium-rich material from a non-degenerate or degenerate companion (from a helium star or a helium-rich white dwarf, **or from the pre-existing thin helium layer on top of a carbon-oxygen white dwarf** in merger events [21–23]). In this helium layer, a detonation is triggered, either by compressional heating when the helium layer (or shell) becomes sufficiently massive, or due to dynamical instabilities [24–27]. This first detonation propagates through the helium shell and drives a shock wave into the carbon-oxygen core where it focuses spherically into a small volume. The compression and heating of the carbon-oxygen material in this region initiates a secondary detonation in the core material and successfully explodes the sub-Chandrasekhar mass white dwarf [28].

Although numerous simulations indicate that the double-detonation mechanism is feasible, **so far they have** failed to resolve the spatial length scales on which the primary helium detonation ignites [29, 30]. While unable to demonstrate the ignition of the required detonations, these simulations do provide us with critical information about the structure, morphology and early time spectra of a double-detonation Type Ia supernova if the ignitions of both detonations are successful.

One observational signature supporting the double-detonation mechanism includes the detection of intermediate mass elements at appropriately high velocities, and plausible evidence for double-detonation events has been previously discussed in the context of high velocity features (HVFs) [9, 31, 32]. The HVFs of Ca II and Si II were studied in a sample of 445 SNe at epochs up to 5 days past maximum brightness [33]. HVFs of Ca II were found in almost two-thirds of the [33] sample, but interestingly such features were absent from the 91bg-like (faint) sub-class of SNe Ia. [Ca II] has also been observed at later times in the spectra of SN 2019yvq [34, 35], SN 2018byg [36] and SN 2016hnk[37]. To date, supernova SN2018byg is widely-acknowledged as one of the most compelling cases in linking the double-detonation mechanism to a SNe Ia explosion, and is best-explained by a model that incorporates a rather massive helium shell [36].

In terms of double-detonation nucleosynthesis, the detonations in the carbon-oxygen core and the helium-rich shell result in qualitatively different **yield products**. This should not come as a surprise, since both the types of fuel (carbon/oxygen vs. helium) and the densities (higher density in the core and lower density in the shell) differ substantially, **by about 2 orders of magnitude**. In the core, the density of the fuel is the key parameter that determines the outcome of the explosive nuclear burning. For densities greater than $\approx 7 \times 10^6\,\mathrm{g\,cm^{-3}}$, the burning is nearly complete, and iron-group elements (IGEs), especially the radioactive ^{56}Ni nucleus, dominate the nucleosynthetic yields. At the "intermediate" densities further off-center in the core, the nuclear fusion time-scale becomes increasingly longer and the rapid expansion of the white dwarf leads to a freeze-out of the nuclear reactions before burning to IGEs is completed. As a result, the synthesis of intermediate-mass elements (IMEs) dominates these regions, with heavier IMEs like calcium relatively more abundant further inside and lighter IMEs like silicon or sulphur becoming relatively more abundant as the fuel density further decreases outward. Eventually the density becomes too low ($\approx 3 \times 10^6\,\mathrm{g\,cm^{3}}$) for oxygen to burn and only carbon continues to burn to light IMEs like oxygen, neon, and magnesium. A recent review [38] shows a schematic of this well known layered structure.

At even lower densities, the fuel composition rapidly changes where the helium shell begins. Importantly, owing to its lower Coulomb barrier, helium (^{4}He) is more reactive, and helium detonations are possible down to much lower densities [39]. Similar to the carbon-oxygen core, helium-shell detonations produce a radially layered progression in the atomic weight of the burning products, with the heavier elements like chromium, iron, or nickel preferentially synthesized at the inner, denser parts of the shell; lighter elements like unburned helium, carbon, or oxygen are found at the outer, less dense parts of the shell, and intermediate-mass elements like silicon or sulphur in between [40] (see Extended Data Fig. 1). For **optimal** agreement with observations (in particular the colours **in synthetic lightcurves**), it is important that the density at the base of the helium shell is not too large (less than $\sim 10^6\,\mathrm{g\,cm^{-3}}$), such that the production of IGEs in the He-shell is limited and intermediate-mass elements like calcium are the most abundant nucleosynthesis products at the base of the helium shell [27, 32].

Therefore, taking the nucleosynthetic signatures of the CO core and the He-shell together, double-detonation models predict calcium to be concentrated in two separate layers: an inner layer from the core **region**, corresponding to the incomplete burning of the CO-detonation (at fuel densities around a few $\times 10^6\,\mathrm{g\,cm^{-3}}$), and an outer layer at higher velocity in the expanding explosion ejecta, corresponding to the base of the He-shell (fuel densities around a few $10^5\,\mathrm{g\,cm^{-3}}$). Explosion models, including the M10_03 model by Collins et al. [41] (see Fig. 2 in Extended Data) predict such *a double shell morphology of Ca*, with intermediate mass elements lighter than Ca, such as S or Si, located in between the two shells.

While numerical simulations alone cannot confirm that the double-detonation mechanism occurs in nature, a confirmed observation of the tell-tale two-shell structure would supply direct **evidence** for its operation in Type Ia supernovae. However, the unique **double shell Ca morphology** "fingerprint" structure remains inaccessible at the epochs around peak luminosity (15 to 20 days after explosion) because the inner part of the expanding ejecta is opaque to optical light and the object remains a spatially unresolved point source. This, however, changes with time **as the supernova continually expands**. Here we present **a new piece of** compelling evidence – a "photographic snapshot" – that SNe Ia can explode via the double-detonation mechanism. **The evidence is** based on deep MUSE integral field observations of the reverse shocked ejecta of the supernova remnant SNR 0509-67.5 (hereafter SNR 0509).

From light echo observations, SNR 0509 is known to be part of the SN1991T-like (more luminous than average at peak brightness) sub-class of SNe Ia [42, 43]. It is very young ($\sim 300-350$ yrs [44]) and located in the nearby Large Magellanic Cloud (LMC), granting us an exclusive view into the early stages of the evolution of a Type Ia SNR. **A few hundred years after the explosion, the inner part of the expanding ejecta is exposed by shock waves in the supernova remnant [45] and can be spatially resolved in astronomical observation.** The ejecta of SNR 0509 is expanding in a low-density ambient medium, as evidenced by the near-spherical symmetry of the forward shock. Detailed tomography and modelling of the emission of the reverse shocked ejecta in this system has been performed [45], which reported the discovery of [Fe XIV]5303, and excesses indicating the presence of [Fe IX]8235, [Fe XV]7060, as well as [S XII]7611. The resulting new constraints from the location of the optical emission of the reverse shocked ejecta and a set of analytical hydrodynamical supernova remnant models [45] were used to argue that the SN1991T-like event forming this SNR should have been an energetic sub-Chandrasekhar mass explosion [46]. Following the discovery of the optically-emitting reverse shocked ejecta, our team conducted deeper optical observations of SNR 0509, which now reveal the shocked ejecta in greater detail (see Fig. 1 for a sample spectrum extracted from the western side of the remnant). In addition to the emission lines detected previously, we now also detect [Fe IX]4967, [Fe X]6375, [Fe XI]7892, and possibly [Ni XIII]4950. Importantly, we also observe broad [Ca XV]5695. The morphology of this calcium line relative to the sulphur emission reveals important clues about the nature of the supernova explosion mechanism.

Specifically, we report here the discovery in SNR 0509 of a double shell structure of highly-ionized [Ca XV] alongside a single shell of [S XII] emission from the supernova ejecta (see Fig. 2). The inward propagating reverse shock progressively ionizes the ejecta material, exhibiting optical forbidden line emission from these highly ionized atoms of calcium and sulphur. Thus, the observed shell structures of calcium and sulphur reflect the morphological distribution of the ejecta material. The observed shell structures of these species are comparable (since the SNR is still young and expanding into a low density ambient medium [46]) with the column density structures of the same elements in the M10_03 model [26]. M10_03 is a hydrodynamical explosion model of a double-detonation with a carbon-oxygen-rich core mass of 1.028 $M_\odot$ and a He-shell mass of 0.027 $M_\odot$. The double-shell structure of ^{40}Ca evident in Fig. 2 (**see also Fig. 3 for overlay**) is a signature of the double-detonation explosion scenario, where the outer Ca-shell is formed due to the burning of the He shell and the inner Ca-shell is formed due to burning of the carbon–oxygen core. By showing surface brightness contours, Fig. 4 illustrates the double shell structure of calcium (cyan), with sulphur (red) peaking in between the two calcium shells, and the Balmer emission behind the forward shock which is much further out (magenta). **The position of the Balmer emission marks the shocked CSM and the observed [Ca XV] along with the [S XII] are positioned behind the forward shock. We stress again the fact that these observed emission lines of highly-ionized [Ca XV] come from the ejecta that have been shocked by the (radially inward-propagating) reverse shock. The width of the Gaussian profile is proportional to the reverse shock speed. The narrow line width of the**

outer shell compared to the broader inner shell indicates that the reverse shock speed increases as it travels inwards, possibly due to clumping of the ejecta. The peak of the sulphur emission as observed is spatially located between the inner and outer calcium shells, **closer to the outer shell** (see Fig. 4 upper centre), which follows the structural morphology of the M10_03 model with remarkable similarity (see Fig. 1, Extended data). **We attribute the partial overlap of the sulphur and outer calcium shells to atmospheric seeing. Our spectral analysis and modelling show** that within uncertainties, the Doppler shifts of the inner and outer calcium shells are similar to one another (see section Emission Line Fitting). This provides evidence that we are looking at two limb-brightened shells of calcium (see analysis), as predicted by the double-detonation explosion scenario.**The surface brightness of the double-shell structure of [Ca XV] peaks at two radii: at** $1.73 \pm 0.07\,\mathrm{pc}$ **and** $2.06 \pm 0.07\,\mathrm{pc}$ **from the remnant's centre. Although the observations reported here qualitatively match the signature of the double-detonation explosion model, we do not imply that the chosen model is quantitatively reproducing the observations precisely. We selected this existing double-detonation model as an archetype to compare the tell-tale morphological structure of the detonations, without fine-tuning the model to achieve a best-matching fit.**

The proper motion of the forward shock has been reported to be $\sim 6500\,\mathrm{km/s}$ **[47], unsurprisingly significantly smaller than the ejecta velocity of** $\sim 25000\,\mathrm{km/s}$ **of the fiducial model from [26]. The simulated model only tracks the ejecta for 100s after the explosion, whereas the observed remnant is a few centuries older. The significant decrease in the expansion velocity is due to the remnant interacting with the circumstellar medium. This also reduces the radial extent of the ejecta and the distances between the respective shells in the supernova remnant predicted under the assumption of pure free-expansion.**

The spatial morphology of the observed distribution of the sulphur and calcium lines match what would be expected of a double-detonation of a white dwarf just above 1 solar mass harbouring a thin (low-mass, e.g. ∼0.03 solar masses) helium shell. We thus conclude that SNR 0509 was the result of a double-detonation initiated in a low-mass helium-shell of a sub-Chandrasekhar mass WD progenitor. This is the first direct **photographic evidence of the morphological signature of a specific explosion mechanism in the remnant phase for a Type Ia supernova.**

Our observation provides novel and compelling evidence from the supernova remnant phase, and contributes to resolving the long-standing debate as to whether a Type Ia supernova explosion is possible from a sub-Chandrasekhar mass white dwarf with a thin helium-shell. By extension, this implies that **some** 1991T-like SNe are plausibly explained by double-detonations of sub-Chandrasekhar mass WDs. **The highest-mass explosion model from [26] produced** $0.84 M_\odot$ **of** ^{56}**Ni, which is within the predicted range for 91T-like SNe Ia [13]. Recent observations of SN 2022joj and SN 2020eyj hints towards the possibility of a 91T-like event from the double-detonation of a CO WD [48, 49]. Further reports on observations of SN 2020eyj – classified as a 1991T-like event with evidence of helium-rich circumstellar material – have been speculated to be as a consequence of the double-detonation mechanism [50]. Despite the heavy limitations on 3D simulation capability, and to date no explosion model can adequately explain 91T-like SNe, recent radiative transfer simulations that incorporate non-local thermodynamic**

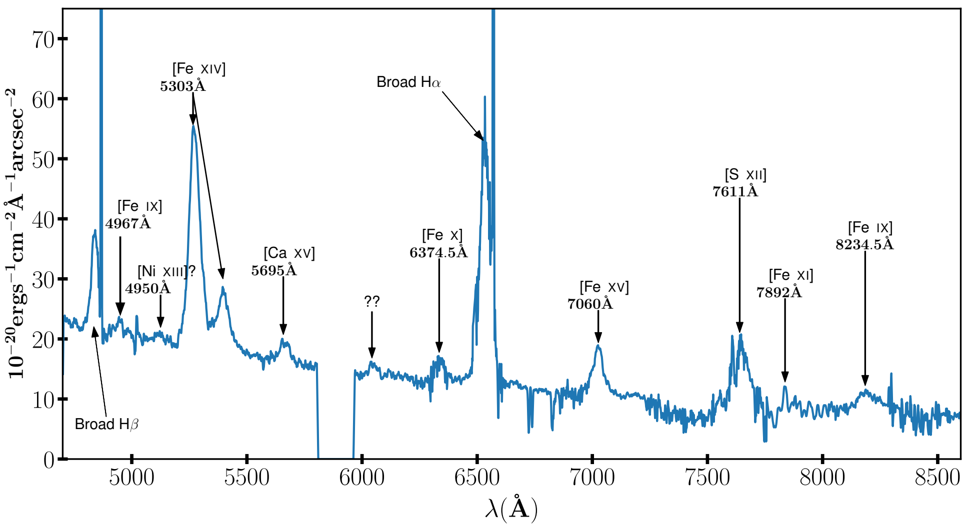

Fig. 1 Spectrum extracted from a region on the western side of the SNR 0509 (region inside the right white rectangle in Fig 2). Seen are broad coronal lines of different ionization states of iron, calcium, and sulfur (and possibly nickel) from the reverse shocked ejecta as well as broad and narrow Balmer lines from the forward shock. The gap in the spectrum around 589 nm stems from the MUSE notch filter used to block the residual laser light from the 4LGSF system (see Sec. 2.1 of the Methods section for details).

equilibrium (NLTE) physics show more promise. It was recently reported that heavy elements in higher ionization states reduce absorption effects, thus bringing a wider range of He shell masses into better agreement with observed SN Ia spectra [51, 52].

While our observations prove the double-detonation mechanism is capable of triggering an explosion in a white dwarf star, both double-degenerate and single-degenerate origins remain possible for the evolutionary scenario [53, 54]. **Recent multidimensional double-detonation simulations [23, 55–57] show that in the white dwarf merger scenario, in addition to the primary WD undergoing a double-detonation, the companion WD can also undergo a double-detonation (resulting in a 'quadruple detonation') upon being impacted by ejecta from the exploding primary WD. Such a double-double-detonation could possibly also lead to the observed double shell structure of calcium. However, self-consistent calculations of the predicted coronal line emission of the reverse shocked ejecta do not yet exist for any explosion model. While we are therefore currently unable to conclusively differentiate between the different variants of double-detonations, we can say that some form of double-detonation leads to Type Ia supernovae.**

Our discovery marks the unique capability of supernova remnant tomography of the reverse shocked ejecta; similar methods of observation can be extended to other young Type Ia supernova remnants. Observations of spatially-resolved inner ejecta are not possible during the explosion itself due to the high opacity and compactness of the material. However, after the ejecta have expanded, it is possible to attain a resolved view of the nucleosynthesis and structural distribution that arose as a consequence of the Type Ia supernova explosion.

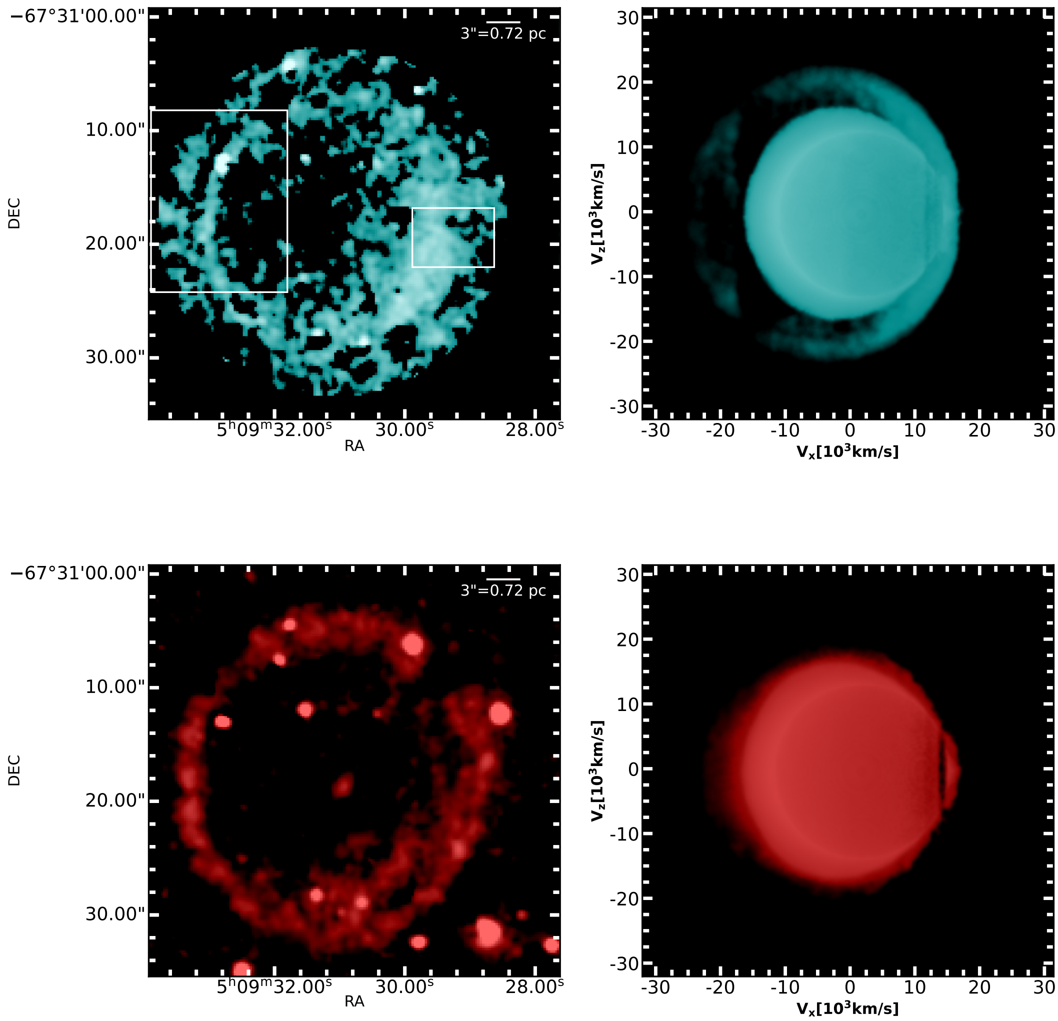

Fig. 2 Top-left: Reverse shocked ejecta emitting in [Ca XV] in SNR 0509 obtained by integrating over a slice from 5626Å to 5752Å (for more details, see Data Visualisation and Analysis). The area within the Eastern (left) white highlighted rectangle shows the region picked for examining the double shell structure. The region within the Western (right) rectangle is the extraction aperture for the spectrum shown in Fig. 1. Top-right: **Integrated column (along the line of sight) of density** $\times$ **density** $\times$ **X(Ca)**, which shows a double shell structure of calcium in the model M10_03 after 100s of explosion. Bottom-left: Reverse shocked ejecta emitting in [S XII] in SNR 0509, obtained by integrating over a spectral slice from 7502Å to 7726Å. The bright point sources in the figure are not sulphur clumps but rather stars that have strong emission lines in the wavelength range of [S XII] (for more details, see analysis). A highly red-shifted background galaxy can be observed at the same wavelength in the centre of the remnant as a diffuse red spot. Bottom-right: **Integrated column of density** $\times$ **density** $\times$ **X(S)**, which shows a single shell structure of sulphur in the model M10_03.

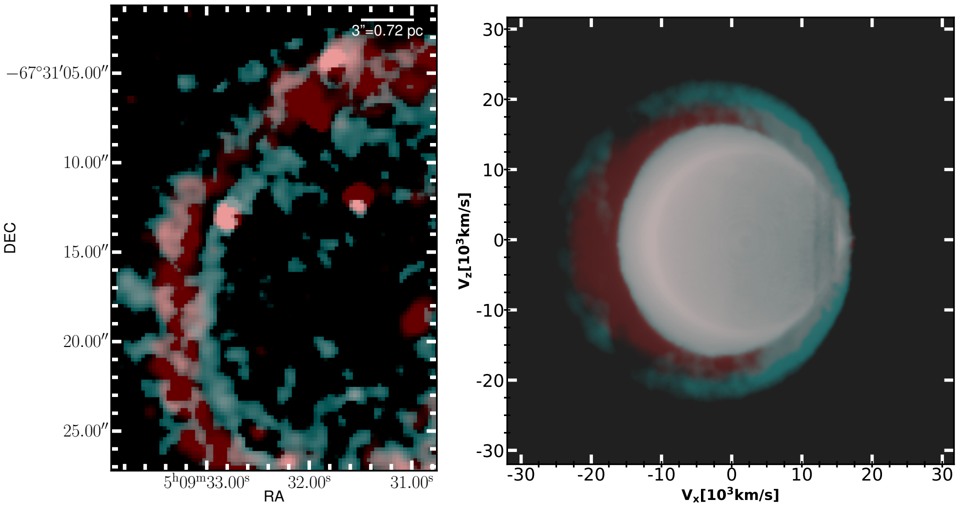

Fig. 3 Left: Spatial distribution of [S XII] (red) and [Ca XV] (cyan) in the ejecta, overlaid together as observed in the Eastern side of the remnant. We detect the presence of sulphur as a single shell that peaks between the two shells of [Ca XV]. Right: Overlay of **the integrated column of density** × **density** × **X(S)(red) and X(Ca) (cyan)** from the M10_03 model showing the presence of sulphur in between the double shells of calcium.

Detailed forward modelling of supernova remnant evolution that calculates the ejecta ionization and excitation structure for 300 – 800 years after explosion holds great promise to make significant advances in understanding the diverse origin of Type Ia supernova progenitors.

References

1. Maoz, D. & Graur, O. Star Formation, Supernovae, Iron, and α: Consistent Cosmic and Galactic Histories. **848,** 25. arXiv: 1703.04540 [astro-ph.HE] (Oct. 2017).
2. Hillebrandt, W., Kromer, M., Röpke, F. & Ruiter, A. Towards an understanding of Type Ia supernovae from a synthesis of theory and observations. *Frontiers of Physics* **8,** 116–143 (2013).
3. Nomoto, K., Thielemann, F. .-. & Yokoi, K. Accreting white dwarf models for type I supern. III. Carbon deflagration supernovae. **286,** 644–658 (Nov. 1984).
4. Khokhlov, A. M. Delayed detonation model for type IA supernovae. **245,** 114–128 (May 1991).
5. Seitenzahl, I. R. *et al.* Three-dimensional delayed-detonation models with nucleosynthesis for Type Ia supernovae. **429,** 1156–1172. arXiv: 1211.3015 [astro-ph.SR] (Feb. 2013).
6. Pakmor, R. *et al.* Sub-luminous type Ia supernovae from the mergers of equal-mass white dwarfs with mass ~0.9M$_{solar}$. **463,** 61–64. arXiv: 0911.0926 [astro-ph.HE] (Jan. 2010).

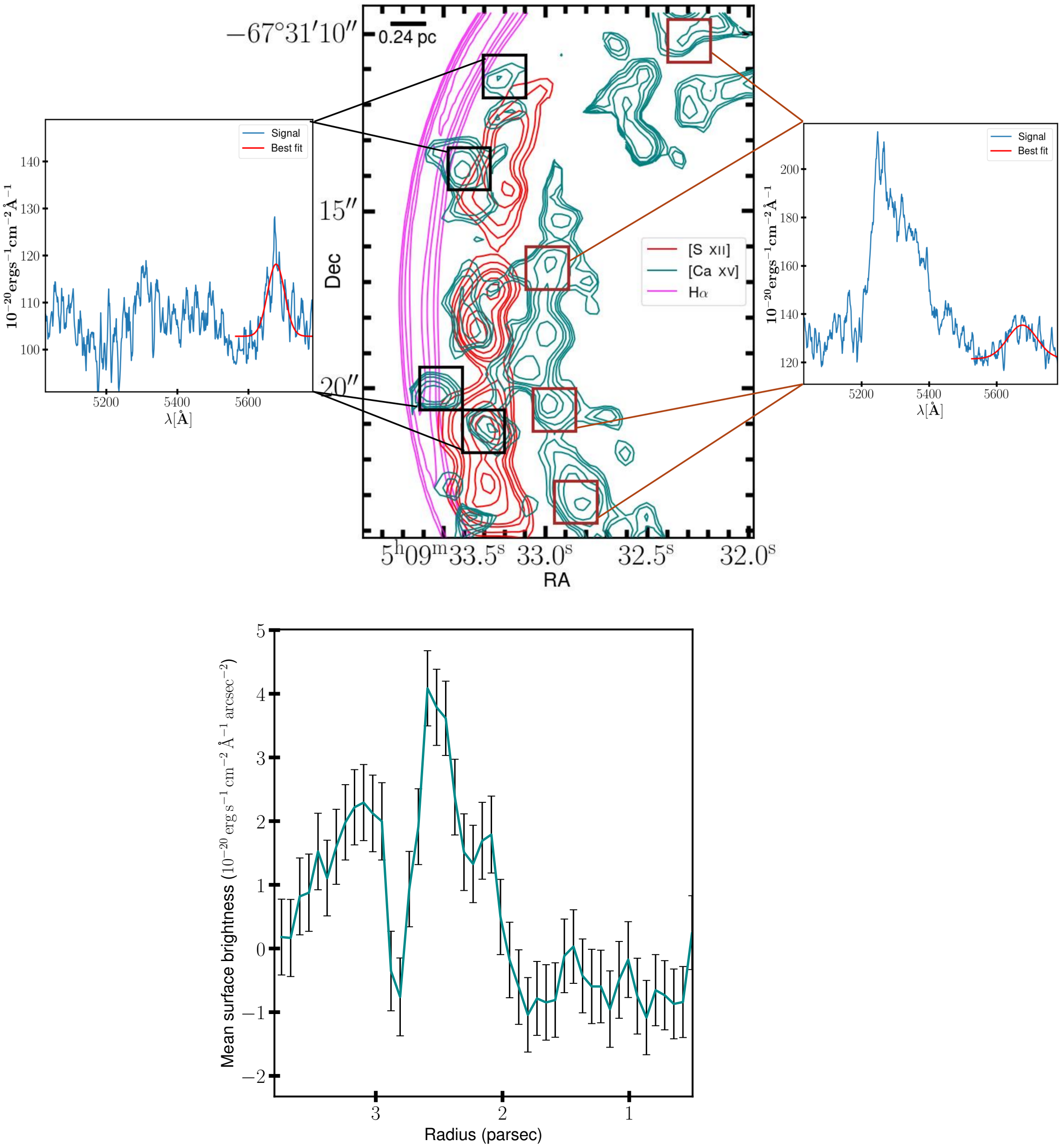

Fig. 4 Upper Left: Spectrum (extracted from the four black squares) showing the Gaussian line fit to [Ca XV] from the outer shell. Upper Centre: Surface brightness contours showing the double shell structure of [Ca XV] (in cyan) and the positioning of [S XII] (in red) between the two calcium shells, with the forward shock (Hα in magenta) further outside, marking the outer extent of the supernova remnant. The contours correspond directly to the observations of [Ca XV] and [S XII] inside the white rectangle on the upper left panel of Fig. 2. Upper Right: Spectrum (extracted from the four maroon squares) showing the Gaussian line fit to [Ca XV] from the inner shell. **Lower: Mean surface brightness of [Ca XV] (integrated over $5632 - 5740$ Å) binned into annuli of 1.5 spaxel vs radius graph for the region indicated by the white rectangle in the eastern side of the remnant (shown in top left pannel of Fig 2) [Ca XV], which shows two peaks corresponding to two shells as seen above with a region of negligible signal in between.**

7. Ruiter, A. J. *et al.* On the brightness distribution of Type Ia supernovae from violent white dwarf mergers. **429,** 1425–1436. arXiv: 1209.0645 [astro-ph.SR] (Feb. 2013).
8. Townsley, D. M., Miles, B. J., Shen, K. J. & Kasen, D. Double Detonations with Thin, Modestly Enriched Helium Layers can Make Normal Type Ia Supernovae. **878,** L38. arXiv: 1903.10960 [astro-ph.SR] (June 2019).
9. Polin, A., Nugent, P. & Kasen, D. Observational Predictions for Sub-Chandrasekhar Mass Explosions: Further Evidence for Multiple Progenitor Systems for Type Ia Supernovae. **873,** 84. arXiv: 1811.07127 [astro-ph.HE] (Mar. 2019).
10. Eitner, P. *et al.* Observational constraints on the origin of the elements. III. Evidence for the dominant role of sub-Chandrasekhar SN Ia in the chemical evolution of Mn and Fe in the Galaxy. **635,** A38. arXiv: 2003.01721 [astro-ph.GA] (Mar. 2020).
11. Ruiter, A. J. & Seitenzahl, I. R. Type Ia supernova progenitors: a contemporary view of a long-standing puzzle. *arXiv e-prints,* arXiv:2412.01766. arXiv: 2412.01766 [astro-ph.SR] (Dec. 2024).
12. Branch, D., Livio, M., Yungelson, L. R., Boffi, F. R. & Baron, E. In Search of the Progenitors of Type IA Supernovae. **107,** 1019 (Nov. 1995).
13. Taubenberger, S. in *Handbook of Supernovae* (eds Alsabti, A. W. & Murdin, P.) 317 (2017).
14. Sim, S. A. *et al.* Synthetic light curves and spectra for three-dimensional delayed-detonation models of Type Ia supernovae. **436,** 333–347. arXiv: 1308.4833 [astro-ph.HE] (Nov. 2013).
15. Wygoda, N., Elbaz, Y. & Katz, B. Type Ia supernovae have two physical width-luminosity relations and they favour sub-Chandrasekhar and direct collision models - I. Bolometric. **484,** 3941–3950. arXiv: 1711.00969 [astro-ph.HE] (Apr. 2019).
16. Sim, S. A. *et al.* Detonations in Sub-Chandrasekhar-mass C+O White Dwarfs. **714,** L52–L57. arXiv: 1003.2917 [astro-ph.HE] (May 2010).
17. Gilfanov, M. & Bogdán, Á. An upper limit on the contribution of accreting white dwarfs to the typeIa supernova rate. **463,** 924–925. arXiv: 1002.3359 [astro-ph.CO] (Feb. 2010).
18. Ruiter, A. J., Belczynski, K. & Fryer, C. Rates and Delay Times of Type Ia Supernovae. **699,** 2026–2036. arXiv: 0904.3108 [astro-ph.SR] (July 2009).
19. Kushnir, D., Katz, B., Dong, S., Livne, E. & Fernández, R. Head-on Collisions of White Dwarfs in Triple Systems Could Explain Type Ia Supernovae. **778,** L37. arXiv: 1303.1180 [astro-ph.HE] (Dec. 2013).
20. Toonen, S., Perets, H. B. & Hamers, A. S. Rate of WD-WD head-on collisions in isolated triples is too low to explain standard type Ia supernovae. **610,** A22. arXiv: 1709.00422 [astro-ph.HE] (Feb. 2018).
21. Iben Jr, I., Nomoto, K., Tornambe, A. & Tutukov, A. V. On interacting helium star-white dwarf pairs as supernova precursors. *The Astrophysical Journal* **317,** 717–723 (1987).
22. Taam, R. E. The long-term evolution of accreting carbon white dwarfs. *Astrophysical Journal, Part 1, vol. 242, Dec. 1, 1980, p. 749-755.* **242,** 749–755 (1980).
23. Pakmor, R. *et al.* On the fate of the secondary white dwarf in double-degenerate double-detonation Type Ia supernovae. **517,** 5260–5271. arXiv: 2203.14990 [astro-ph.SR] (Dec. 2022).

24. Shen, K. J. & Moore, K. The Initiation and Propagation of Helium Detonations in White Dwarf Envelopes. **797,** 46. arXiv: 1409.3568 [astro-ph.HE] (Dec. 2014).
25. Townsley, D. M., Miles, B. J., Shen, K. J. & Kasen, D. Double detonations with thin, modestly enriched helium layers can make normal type Ia supernovae. *The Astrophysical Journal Letters* **878,** L38 (2019).
26. Gronow, S., Collins, C. E., Sim, S. A. & Röpke, F. K. Double detonations of sub-M_{Ch} CO white dwarfs: variations in Type Ia supernovae due to different core and He shell masses. **649,** A155. arXiv: 2102.06719 [astro-ph.SR] (May 2021).
27. Boos, S. J., Townsley, D. M., Shen, K. J., Caldwell, S. & Miles, B. J. Multidimensional Parameter Study of Double Detonation Type Ia Supernovae Originating from Thin Helium Shell White Dwarfs. **919,** 126. arXiv: 2101.12330 [astro-ph.HE] (Oct. 2021).
28. Livne, E. & Arnett, D. Explosions of Sub–Chandrasekhar Mass White Dwarfs in Two Dimensions. *Astrophysical Journal v. 452, p. 62* **452,** 62 (1995).
29. Fink, M., Hillebrandt, W. & Röpke, F. K. Double-detonation supernovae of sub-Chandrasekhar mass white dwarfs. **476,** 1133–1143. arXiv: 0710.5486 [astro-ph] (Dec. 2007).
30. Fink, M. *et al.* Double-detonation sub-Chandrasekhar supernovae: can minimum helium shell masses detonate the core? **514,** A53. arXiv: 1002.2173 [astro-ph.SR] (May 2010).
31. Shen, K. J. *et al.* Three Hypervelocity White Dwarfs in Gaia DR2: Evidence for Dynamically Driven Double-degenerate Double-detonation Type Ia Supernovae. **865,** 15. arXiv: 1804.11163 [astro-ph.SR] (Sept. 2018).
32. Kromer, M. *et al.* Double-detonation sub-Chandrasekhar supernovae: synthetic observables for minimum helium shell mass models. *The Astrophysical Journal* **719,** 1067 (2010).
33. Silverman, J. M. *et al.* High-velocity features of calcium and silicon in the spectra of Type Ia supernovae. **451,** 1973–2014. arXiv: 1502.07278 [astro-ph.HE] (Aug. 2015).
34. Miller, A. *et al.* The Spectacular Ultraviolet Flash from the Peculiar Type Ia Supernova 2019yvq. *The Astrophysical Journal* **898,** 56 (2020).
35. Siebert, M. R., Dimitriadis, G., Polin, A. & Foley, R. J. Strong Calcium Emission Indicates that the Ultraviolet-flashing SN Ia 2019yvq Was the Result of a Sub-Chandrasekar-mass Double-detonation Explosion. *The Astrophysical Journal Letters* **900,** L27 (2020).
36. De, K. *et al.* ZTF 18aaqeasu (SN2018byg): a massive helium-shell double detonation on a sub-Chandrasekhar-mass white dwarf. *The Astrophysical Journal Letters* **873,** L18 (2019).
37. Jacobson-Galán, W. V. *et al.* Ca hnk: The calcium-rich transient supernova 2016hnk from a helium shell detonation of a sub-Chandrasekhar White Dwarf. *The Astrophysical Journal* **896,** 165 (2020).
38. Seitenzahl, I. R. & Townsley, D. M. in *Handbook of Supernovae* (eds Alsabti, A. W. & Murdin, P.) 1955 (2017).
39. Timmes, F. X. & Niemeyer, J. C. Regimes of Helium Burning. **537,** 993–997. arXiv: astro-ph/0005339 [astro-ph] (July 2000).

40. Townsley, D. M., Moore, K. & Bildsten, L. Laterally Propagating Detonations in Thin Helium Layers on Accreting White Dwarfs. **755,** 4. arXiv: 1205.6517 [astro-ph.SR] (Aug. 2012).
41. Collins, C. E., Gronow, S., Sim, S. A. & Röpke, F. K. Double detonations: variations in Type Ia supernovae due to different core and He shell masses–II. Synthetic observables. *Monthly Notices of the Royal Astronomical Society* **517,** 5289–5302 (2022).
42. Rest, A. *et al.* Spectral Identification of an Ancient Supernova Using Light Echoes in the Large Magellanic Cloud. **680,** 1137–1148. arXiv: 0801.4762 [astro-ph] (June 2008).
43. Badenes, C., Hughes, J. P., Cassam-Chenaı, G. & Bravo, E. The Persistence of Memory, or How the X-Ray Spectrum of SNR 0509-67.5 Reveals the Brightness of Its Parent Type Ia Supernova. **680,** 1149–1157. arXiv: 0801.4761 [astro-ph] (June 2008).
44. Rest, A. *et al.* Light echoes from ancient supernovae in the Large Magellanic Cloud. **438,** 1132–1134. arXiv: astro-ph/0510738 [astro-ph] (Dec. 2005).
45. Seitenzahl, I. R., Ghavamian, P., Laming, J. M. & Vogt, F. P. Optical tomography of chemical elements synthesized in type Ia supernovae. *Physical review letters* **123,** 041101 (2019).
46. Arunachalam, P., Hughes, J. P., Hovey, L. & Eriksen, K. A Hydro-based MCMC Analysis of SNR 0509-67.5: Revealing the Explosion Properties from Fluid Discontinuities Alone. **938,** 121. arXiv: 2208.07693 [astro-ph.HE] (Oct. 2022).
47. Hovey, L., Hughes, J. P. & Eriksen, K. A Direct Measurement of the Forward Shock Speed in Supernova Remnant 0509-67.5: Constraints on the Age, Ambient Density, Shock Compression Factor, and Electron-ion Temperature Equilibration. **809,** 119 (Aug. 2015).
48. Liu, C. *et al.* SN 2022joj: A Peculiar Type Ia Supernova Possibly Driven by an Asymmetric Helium-shell Double Detonation. **958,** 178. arXiv: 2308.06319 [astro-ph.HE] (Dec. 2023).
49. Gonzalez, E. P. *et al.* SN 2022joj: A Potential Double Detonation with a Thin Helium Shell. *The Astrophysical Journal* **964,** 196 (2024).
50. Kool, E. C. *et al.* A radio-detected type Ia supernova with helium-rich circumstellar material. *Nature* **617,** 477–482 (2023).
51. Collins, C. E. *et al.* Non-LTE radiative transfer simulations: Improved agreement of the double detonation with normal Type Ia supernovae. *arXiv e-prints,* arXiv:2411.11643. arXiv: 2411.11643 [astro-ph.SR] (Nov. 2024).
52. Boos, S. J., Dessart, L., Shen, K. J. & Townsley, D. M. Non-LTE Synthetic Observables of a Multidimensional Model of Type Ia Supernovae. *arXiv e-prints,* arXiv:2410.22276. arXiv: 2410.22276 [astro-ph.HE] (Oct. 2024).
53. Ruiter, A. J., Belczynski, K., Sim, S. A., Seitenzahl, I. R. & Kwiatkowski, D. The effect of helium accretion efficiency on rates of Type Ia supernovae: double detonations in accreting binaries. **440,** L101–L105. arXiv: 1401.0341 [astro-ph.SR] (May 2014).
54. Kool, E. C. *et al.* A radio-detected type Ia supernova with helium-rich circumstellar material. **617,** 477–482. arXiv: 2210.07725 [astro-ph.HE] (May 2023).
55. Shen, K. J., Boos, S. J. & Townsley, D. M. Almost All Carbon/Oxygen White Dwarfs Can Support Double Detonations. *arXiv preprint arXiv:2405.19417* (2024).

56. Tanikawa, A., Nomoto, K., Nakasato, N. & Maeda, K. Double-detonation Models for Type Ia Supernovae: Trigger of Detonation in Companion White Dwarfs and Signatures of Companions' Stripped-off Materials. **885,** 103. arXiv: 1909.09770 [astro-ph.HE] (Nov. 2019).
57. Boos, S. J., Townsley, D. M. & Shen, K. J. Type Ia Supernovae Can Arise from the Detonations of Both Stars in a Double Degenerate Binary. **972,** 200. arXiv: 2401.08011 [astro-ph.HE] (Sept. 2024).

2 Methods

2.1 Observations and data reduction

SNR 0509 was observed with the MUSE [1] optical integral field spectrograph, which is mounted on the Unit Telescope 4 (UT4) of the European Southern Observatory (ESO) Very Large Telescope on Cerro Paranal, under ESO program ID 0104.D-0104(A) (P.I.: Seitenzahl). The data were acquired in service mode with the WFM-AO setup over 25 distinct nights spread over 24 months (see Table 2.1 for details). **A total of** 39 **individual** observations have an exposure time of $\sim$ 2700 s each **(corresponding to total exposure time of** $\sim$**105300 s = 29 h and 15 min on-source)**, while a single observation **(that was ignored in our analysis) has an exposure time of 93.92 s**. In the WFM-AO mode, MUSE data spans the optical wavelength range from 4690 Å to 9340 Å with a resolution of R$\sim$3000. **This mode relies on the UT4 Adaptive Optics Facility [2, AOF], which is comprised of a deformable secondary mirror [3], the AO modules GRAAL [4] and GALACSI [5] (of which only the latter is relevant for MUSE operations), and the 4 Laser Guide Star Facility [6, 4LGSF] that is responsible for the creation of artificial guide stars by means of four 22 W sodium lasers. When MUSE is observing in any of its AO mode, a notch filter centered around the lasing wavelength of 589 nm is inserted in the scientific light path to avoid the contamination of data by scattered laser light**[1]. **The dip in the spectrum presented in Fig. 1 is a direct consequence of this notch filter.**

We use ESOReflex [**Freudling2013**] version 2.11.5, and the MUSE data reduction pipeline version '2.8.9' [11] to perform a standard data reduction of our data. The standard reduction was performed using the default settings, which removes the standard and known skylines from the data. This reduction was performed on Tycho, a large memory Linux workstation at the University of New South Wales in Canberra specifically designed for data reduction of MUSE observations. Using the MUSE pipeline, all 39 individual MUSE pixel tables were stacked together into the final mosaic analyzed and discussed in this article, which has a size of 1 arcmin $\times$ 1 arcmin, with a spaxel size of 0.2 arcsec $\times$ 0.2 arcsec.

2.2 Data processing and sky subtraction

Standard pipeline data reduction using EsoReflex performs background sky subtraction either by using pre-calculated skylines and continuum if dedicated sky observations are available or by computing a sky from the fraction of the field of view specified by the parameter SkyFr_2. The latter option is used in the present case. The residual skylines present in the final

[1]The notch filter does not prevent the contamination of MUSE observations by Raman-scattered laser photons [see 7–10, for details]. These emission lines are cleaned up by the MUSE data reduction pipeline [11].

mosaic remain problematic, given the low-flux scientific signals from the shocked ejecta. We have therefore implemented an additional "local background" subtraction approach to further minimize these residual skylines, and help with the analysis of the faint broad signals in the spectrum, similarly to [12]. The background selection was performed locally using QFitsView. Eight local background regions were selected from the white-light image, avoiding stellar or SNe ejecta contamination. These areas are usually small ($\sim 30 - 40$ spaxels), since the field is crowded with stars, and away from the SNR 0509 center as shown in Fig. 3.

The combined datacube (MUSE DEEP) has been corrected for Galactic extinction along the line-of-sight using a customized brutifus (https://github.com/brutifus) procedure. We use a Fitzpatrick (1999) reddening law [13] with $R_V = 3.1$, $A_B = 0.272$, and $A_V = 0.206$, obtained through NED from a re-calibration[14] of the infrared-based dust map [15].

2.3 Data analysis and visualization

The highly ionized calcium ([Ca XV]) in the reverse shocked ejecta is visualized in the upper left panel of Fig. 2 of the main article. We have integrated the spectrum from 5626Å to 5752Å, where we observe the [Ca XV] signal ($\lambda_0 = 5694.80$). A continuum is subtracted by selectively choosing and integrating the spectrum ranging from 5591Å to 5608Å and from 5759Å to 5802Å to minimise stars and residual noise. Since the flux of the broad emission line of calcium is very low, comparable to the background noise, we have visualized the sliced data cube of calcium using a log colour scale. To minimize distracting artificial features from bright stars, we have also only visualized the region inside the forward shock (as delineated by the Hα shell), since **no ejecta is present** outside of the forward shock **for SNR 0509 [16, 17]** (the signal outside the forward shock is set to zero). The sulphur in the lower left panel of Fig. 2 has been visualized by a similar process of integrating the spectrum from 7502Å to 7726Å and subtracting a continuum on both sides of the signal (7399Å to 7434Å and 7716Å to 7827Å). Although this procedure works well to subtract the stellar continuum, the resultant [S XII] signal is still left with some residual stellar emission line exactly at the same wavelength range selected for its visualization. Due to this, there are few bright stars appearing as bright blobs in [S XII].

We have also analyzed the hydrodynamical explosion model M10_03 [18] to compare the structural signatures of calcium and sulphur, formed as a result of the double-detonation supernova event. As the SNR 0509 is a young remnant, the reverse shock has not yet reached the center of the remnant, and thus the calcium and sulphur are ionized to some extent from the rim. We have calculated the ratio of the radius of the outer shell of [Ca XV] (3.53 parsec) and the inner radius of [Fe IX] (2.52 parsec) which is ≈ 1.4. The inner radius of [Fe IX] in the observed ejecta marks the inward extent of the reverse shock. Since SNR0509 is a young Type Ia remnant, the reverse shock has not yet reached the centre of the explosion. The radii were calculated by fitting circles on the outer shell of [Ca XV] and the shell of [Fe IX] in SAOIMAGE DS9 [19]. This ratio is then used to find the inner radius of calcium and sulphur in the model. The density of the elements inside the inner radius has been masked to mimic the extent of the reverse shock from the rim toward the center in the observation. We **plotted the integrated (along the line of sight) column of density $\times$ density $\times$ mass fraction of calcium and sulphur, respectively. We have chosen this quantity for comparing with the observations (see Fig 2) because the surface brightness of the coronal lines should scale with the collision rate, which is proportional to electron density and species ion density.**

For a highly ionized medium, the electron density n_e is proportional to the total particle density, giving us the density $\times$ density $\times$ mass fraction scaling.

Fig. 4 (upper center) shows the Balmer emission (Hα) due to forward shock and reverse shocked ejecta in terms of surface brightness contour levels. Hα (in green) contours are given by (0.884, 0.977, 1.135, 1.254, 1.457) $10^{-15}\,\mathrm{erg\,s^{-1}\,cm^{-2}\,\AA^{-1}\,arcsec^{-2}}$, the levels of [S XII] are given by (1.080, 1.255, 1.533, 1.694, 2.070, 2.404, 2.657) $10^{-17}\,\mathrm{erg\,s^{-1}\,cm^{-2}\,\AA^{-1}\,arcsec^{-2}}$ and the [Ca XV] contours are (1.974, 2.411, 2.944, 3.975, 4.854, 6.889]) $10^{-18}\,\mathrm{erg\,s^{-1}\,cm^{-2}\,\AA^{-1}arcsec^{-2}}$. The contour levels are chosen in the image created using the integration of the surface brightness per spaxel, over the binned wavelength containing their respective signals. The contours with smaller areas represent regions of higher surface brightness in contrast to larger contour areas. The formation of several small contour regions in [S XII] and [Ca XV] marks the presence of small regions with very high surface brightness, caused by the formation of high-density blobs (clumping of the ejecta) in the reverse shocked ejecta. Whereas the forward shock (Hα) is much smoother with no presence of clumping. The above operations were carried out by the python package Astropy [20, 21] and visualized with Matplotlib [22].

Fig, 4 (lower) shows the mean surface brightness of [Ca XV] in annular bins on the y-axis against radius on the x-axis. The region of SNR 0509 in the North-East exhibiting the double shell morphology most clearly is considered for the operation. The data are binned into annuli of 1.5 spaxel width, with the centre of the annuli at RA = $05\mathrm{h}\,09\mathrm{m}\,31.0\mathrm{s}$ **and DEC =** $-67°31'18''$**. We masked areas most affected by stars by considering the increase in the average flux of the spectrum above** $5\times10^{-20}\,\mathrm{erg\,s^{-1}\,cm^{-2}\,\AA^{-1}\,arcsec^{-2}}$**. This approach was necessary to minimize the contamination from any star as the tool `Brutifus` is unable to subtract stellar signals in these broad coronal lines.**

2.3.1 Ionization effect on ejecta

We investigate the ionization fractions in the densest part of the SNR model for 0509–67.5 favored in recent research [23]; 1.5×10^{51} ergs explosion energy, 1 $\mathrm{M_\odot}$, and 0.4 $\mathrm{amu/cm^3}$ interstellar medium density. Using an outer envelope power law of 7 for the outer $3/7$ of the ejecta by mass, the densest ejecta are found at this boundary. Here, [Fe XIV] forms without any clumping, at an ionization age $\mathrm{n_{et}} = 2\times10^9\ \mathrm{cm^{-3}\,s}$, but is maximized in ionization fraction for about a factor of $1.5\times$ clumping in density. [S XII] requires $1.5-3\times$ clumping, and [Ca XV] needs $3-5\times$ density enhancement. The fact that [S XII] forms where the ejecta are predicted to be the densest, and [Ca XV] form either side strongly implies stratification of element abundances rather than an ionization effect. This clumping most plausibly arises as radioactive Ni-Co formed in the explosion expands and compresses the non-radioactive surroundings, and is consistent with the lack of clumping required for [Fe XIV].

2.4 Emission line fitting

We have selected 4 regions from each of the suspected double shell structures of the [Ca XV] from the eastern region, where it is more distinctly visible. The spectra from the outer shell (black squres) and inner shell (maroon squares) regions are summed independently to improve the signal/noise ratio. Each region is $\sim 3\times3$ spaxel, shown in Fig. 4 (upper center) of the main-text. We have used the Gaussian function with a defined constant and the `curve_fit` function from `Scipy.signal` to fit the signal. The `curve_fit` function returns the optimum parameters after fitting and the associated covariance for the values from which the errors are calculated.

We calculated the Doppler shift for both apparent shells of [Ca XV] to ensure that they are **distinct structures having different distances from the remnant centre, and are not simply two different regions located on different areas of the same spherical shell but having the same physical distance from the remnant's centre. The latter might give in projection a false impression of a double shell structure. We can test for and rule out such a scenario by measuring the Doppler shift of the inner shell in comparison to the outer shell. If both arcs are situated at a similar radius (i.e., they are different regions of the same spherical shell), then the inner arc should be significantly Doppler-shifted relative to the outer arc. On the other hand, if both are found to be expanding perpendicular to the line of sight, then we are seeing two limb-brightened separate shells with a correspondingly small Doppler shift between them.**

In Fig. 4 (lower), the surface brightness of the outer and inner shells of calcium peak at a radius of $2.06\,\mathrm{pc}$ **and** $1.73\,\mathrm{pc}$**, respectively, from the geometric centre of the remnant. For simplicity, lets assume that the ejecta is expanding radially outward in spherical symmetry, likely a good assumption given the young age of the remnant and the high degree of spherical symmetry. For the 'projection' case described above where the flux peaks are due to two distinct regions on the *same* expanding shell, the area with smaller (projected) distance from the centre will have a (projected) radius** R_2**, which is related to** R_1 **by the angle** θ **(see Fig 1). Therefore the relation between the two radii due to such a projection effect can be simply defined as** $R_2 = R_1 \cos\theta$**, where** $R_1 > R_2$**. Therefore,** $\theta = 0.57\,\mathrm{radian}$**. Let us assume a conservative radial expansion speed of calcium** $V = 7000\,\mathrm{km/s}$ **(maximum Doppler shift calculated from iron is** $\sim 6000\,\mathrm{km/s}$ **and the calcium is expected to be expanding at a higher speed than iron). Therefore, the Doppler velocity of the ejecta at the observed angle would be** $V_0 = V \sin\theta$ **, which is** $\sim 3800\,\mathrm{km/s}$**. Thus, the expected difference in Doppler velocity considering the two shells as the part of the same sphere would be much higher than what is observed. We therefore rule out the 'projection' scenario, and conclude the calcium peaks, seen clearly in Fig. 4, arise from two physically distinct shell structures.** Thus, a similar Doppler shift represents two limb-brightened edges of the [Ca XV] as predicted in the models and shown in Fig. 2. The peak wavelengths obtained from the fitting parameters are (5677 ± 8)Å and (5676 ± 18)Å for the outer and inner shell, respectively, indicating that the Doppler shift varies very little in both regions: 660 ± 430 km/s **for the outer shell and** 730 ± 950 km/s for the inner shell.

2.5 Data Availability

The raw MUSE data were collected at the European Organisation for Astronomical Research in the Southern Hemisphere, Chile (ESO Programme 0104.D-0104(A)) and are freely available from the ESO archive (https://archive.eso.org/cms.html). The data for the hydrodynamical simulation of the double-detonation explosion mechanism was developed at HITS and is available upon request.

2.6 Code Availability

The codes used are available upon request from the first author.

References

1. Bacon, R. *et al. The MUSE second-generation VLT instrument* in *Ground-based and Airborne Instrumentation for Astronomy III* **7735** (2010), 131–139.
2. Arsenault, R. *et al. The ESO Adaptive Optics Facility under Test* in *Proceedings of the Third AO4ELT Conference* (eds Esposito, S. & Fini, L.) (Dec. 2013), 118.
3. Arsenault, R. *et al. A deformable secondary mirror for the VLT* in *Advances in Adaptive Optics II* (eds Ellerbroek, B. L. & Bonaccini Calia, D.) **6272** (June 2006), 62720V.
4. Paufique, J. *et al. GRAAL: a seeing enhancer for the NIR wide-field imager Hawk-I* in *Adaptive Optics Systems II* (eds Ellerbroek, B. L., Hart, M., Hubin, N. & Wizinowich, P. L.) **7736** (July 2010), 77361P.
5. Stuik, R. *et al.* GALACSI The ground layer adaptive optics system for MUSE. **49,** 618–624 (Jan. 2006).
6. Calia, D. B., Hackenberg, W., Holzlöhner, R., Lewis, S. & Pfrommer, T. The Four-Laser Guide Star Facility: Design considerations and system implementation. *Advanced Optical Technologies* **3,** 345–361 (June 2014).
7. Vogt, F. P. A. *et al.* Detection and Implications of Laser-Induced Raman Scattering at Astronomical Observatories. *Physical Review X* **7,** 021044. arXiv: 1706.07050 [astro-ph.IM] (Apr. 2017).
8. Vogt, F. P. *et al.* Raman-scattered laser guide-star photons to monitor the scatter of astronomical telescope mirrors. *Astronomy & Astrophysics* **618,** L7 (2018).
9. Vogt, F. P. A. *et al.* Rotational and Rotational-Vibrational Raman Spectroscopy of Air to Characterize Astronomical Spectrographs. **123,** 061101. arXiv: 1907.05897 [astro-ph.IM] (Aug. 2019).
10. Vogt, F. P. A. *et al.* Pure-rotational and rotational-vibrational Raman spectrum of the atmosphere at an altitude of 23 km. *Physical Review Research* **5,** 023145. arXiv: 2304.13747 [astro-ph.IM] (June 2023).
11. Weilbacher, P. M. *et al.* The data processing pipeline for the MUSE instrument. **641,** A28. arXiv: 2006.08638 [astro-ph.IM] (Sept. 2020).
12. Ghavamian, P. *et al.* Integral Field Spectroscopy of Balmer-dominated Shocks in the Magellanic Cloud Supernova Remnant N103B. **847,** 122. arXiv: 1705.03086 [astro-ph.HE] (Oct. 2017).
13. Fitzpatrick, E. L. Correcting for the effects of interstellar extinction. *Publications of the Astronomical Society of the Pacific* **111,** 63 (1999).
14. Schlafly, E. F. & Finkbeiner, D. P. Measuring reddening with Sloan Digital Sky Survey stellar spectra and recalibrating SFD. *The Astrophysical Journal* **737,** 103 (2011).
15. Schlegel, D. J., Finkbeiner, D. P. & Davis, M. Maps of dust infrared emission for use in estimation of reddening and cosmic microwave background radiation foregrounds. *The Astrophysical Journal* **500,** 525 (1998).
16. Rest, A. *et al.* Light echoes from ancient supernovae in the Large Magellanic Cloud. **438,** 1132–1134. arXiv: astro-ph/0510738 [astro-ph] (Dec. 2005).

17. Hughes, J. P. *et al.* ASCA Observations of the Large Magellanic Cloud Supernova Remnant Sample: Typing Supernovae from Their Remnants. **444,** L81 (May 1995).
18. Gronow, S., Collins, C. E., Sim, S. A. & Röpke, F. K. Double detonations of sub-M_{Ch} CO white dwarfs: variations in Type Ia supernovae due to different core and He shell masses. **649,** A155. arXiv: 2102.06719 [astro-ph.SR] (May 2021).
19. Joye, W., Mandel, E., Payne, H., Jedrzejewski, R. & Hook, R. *ASP Conf. Ser. Vol. 295, Astronomical Data Analysis Software and Systems XII* 2003.
20. Robitaille, T. P. *et al.* Astropy: A community Python package for astronomy. *Astronomy & Astrophysics* **558,** A33 (2013).
21. Price-Whelan, A. M. *et al.* Binary Companions of Evolved Stars in APOGEE DR14: Search Method and Catalog of 5000 Companions. *The Astronomical Journal* **156,** 18 (2018).
22. Hunter, J. D. Matplotlib: A 2D graphics environment. *Computing in science & engineering* **9,** 90–95 (2007).
23. Seitenzahl, I. R., Ghavamian, P., Laming, J. M. & Vogt, F. P. Optical tomography of chemical elements synthesized in type Ia supernovae. *Physical review letters* **123,** 041101 (2019).
24. Jülich Supercomputing Centre. JUWELS Cluster and Booster: Exascale Pathfinder with Modular Supercomputing Architecture at Juelich upercomputing Centre. *Journal of large-scale research facilities* **7.** http://dx.doi.org/10.17815/jlsrf-7-183 (2021).
25. Collins, C. E., Gronow, S., Sim, S. A. & Röpke, F. K. Double detonations: variations in Type Ia supernovae due to different core and He shell masses–II. Synthetic observables. *Monthly Notices of the Royal Astronomical Society* **517,** 5289–5302 (2022).

2.7 Acknowledgements

AJR acknowledges financial support from the Australian Research Council under award number FT170100243. JML was supported by basic research funds of the Office of Naval Research. The work of FKR is supported by the Klaus Tschira Foundation and by the Deutsche Forschungsgemeinschaft (DFG, German Research Foundation) – RO 3676/7-1, project number 537700965. FKR acknowledges funding by the European Union (ERC, ExCEED, project number 101096243). CEC has received funding from the European Union (ERC, HEAVYMETAL, 101071865) **and the European Union's Horizon Europe research and innovation program under the Marie Skłodowska-Curie grant agreement No. 101152610.**. Views and opinions expressed are however those of the authors only and do not necessarily reflect those of the European Union or the European Research Council Executive Agency. Neither the European Union nor the granting authority can be held responsible for them. The authors gratefully acknowledge the Gauss Centre for Supercomputing e.V. (www.gauss-centre.eu) for funding this project by providing computing time through the John von Neumann Institute for Computing (NIC) on the GCS Supercomputer [24] at Jülich Supercomputing Centre (JSC). SAS acknowledges funding from STFC grant ST/X00094X/1.

2.8 Author Contribution

Conceptualization: I.R.S., P.D.; Telescope proposal and groundwork: I.R.S., A.J.R., F.P.A.V, J.M.L., P.G., S.T., B.J.W.; Data reduction: P.D., I.R.S., J.S., F.P.A.V., N.R.S.; Post processing

Number of Obs.	Date of observation	Exposure time (s)	Airmass	DIMM Seeing at Start (arcsec)
1	8/02/2021	2700	1.364	0.68
2	8/02/2021	2700	1.389	0.49
3	7/02/2021	2700	1.367	0.51
4	7/02/2021	2700	1.397	0.61
5	6/02/2021	2700	1.384	0.37
6	5/02/2021	2700	1.396	0.67
7	16/01/2021	2700	1.402	0.52
8	12/01/2021	2700	1.381	0.72
90	11/01/2021	2700	1.395	0.6
10	10/01/2021	2700	1.396	0.66
11	17/12/2020	2700	1.365	0.53
12	17/12/2020	2700	1.375	0.44
13	16/12/2020	2700	1.375	0.56
14	15/12/2020	2700	1.398	0.53
15	15/12/2020	2700	1.375	0.45
16	14/12/2020	2700	1.406	0.35
17	14/12/2020	2700	1.37	0.61
18	13/12/2020	2700	1.37	0.66
19	13/12/2020	2700	1.394	0.32
20	13/12/2020	2700	1.411	0.49
21	13/12/2020	2700	1.365	0.52
22	12/12/2020	2700	1.365	0.53
23	12/12/2020	2700	1.495	0.46
24	12/12/2020	2700	1.395	0.6
25	12/12/2020	2700	1.369	0.48
26	10/12/2020	2700	1.391	0.67
27	22/11/2020	2700	1.364	0.42
28	20/11/2020	2700	1.367	0.6
29	20/11/2020	2700	1.369	0.47
30	15/11/2020	2700	1.404	0.48
31	14/11/2020	2700	1.441	0.47
32	14/11/2020	2700	1.382	0.51
33	13/11/2020	2700	1.419	0.5
34	13/11/2020	2700	1.371	0.61
35	12/11/2020	2700	1.385	0.51
36	12/11/2020	2700	1.363	0.47
37	16/02/2020	2700	1.456	0.39
38	23/12/2019	2700	1.396	0.37
39	26/11/2019	2700	1.371	0.36

Table 1 Presents the dates of all the nights when the target was observed and information about the quality of Observation.

of the deep cube: P.D., I.R.S., J.S.; MUSE Data Analysis and visualization: P.D., I.R.S., R.S.; Writing-original draft: P.D., I.R.S., F.K.R., A.J.R., J.M.L, with inputs from all the authors; Explosion model data analysis and visualization: C.E.C., S.A.S., P.D., I.R.S., F.K.R., R.P.;

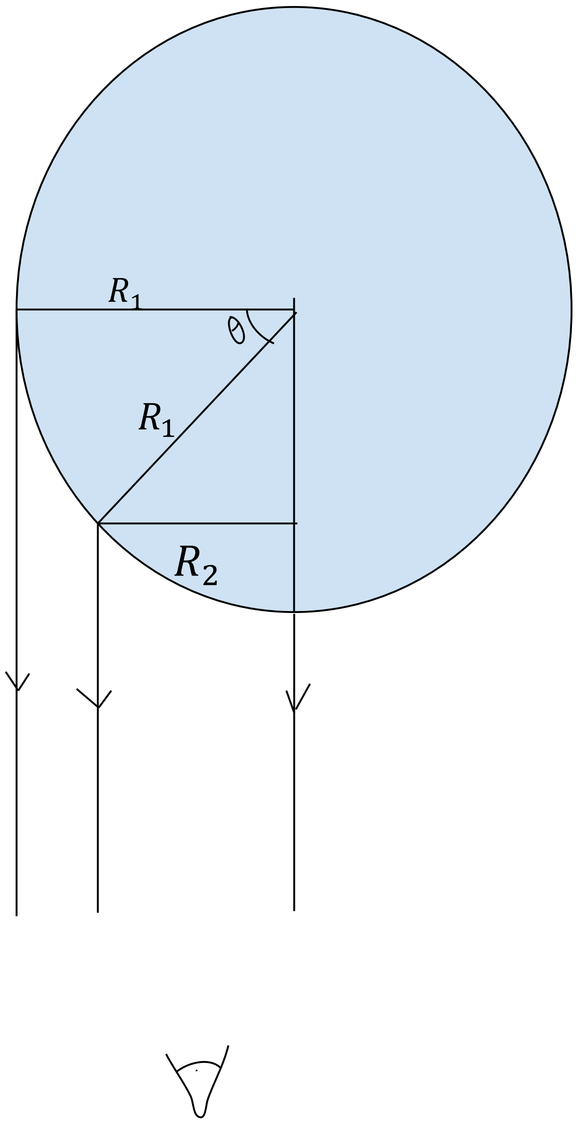

Extended Data Figure. 1 Simple diagram for the visualization of the projection effect affecting the radius of an expanding spherical ejecta

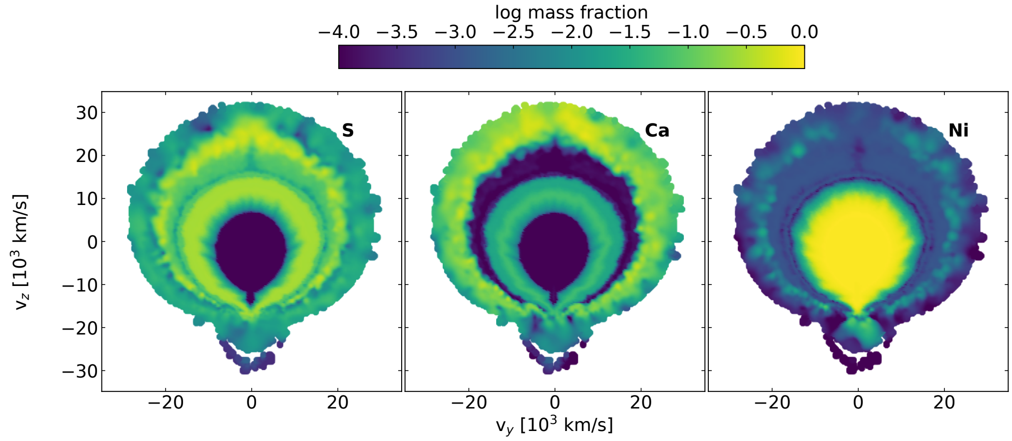

Extended Data Figure. 2 Slices through the y-z plane of the M10_03 double-detonation hydrodynamical explosion model [18, 25] show the distribution of sulfur (left), calcium (middle), and nickel (right) in velocity space.

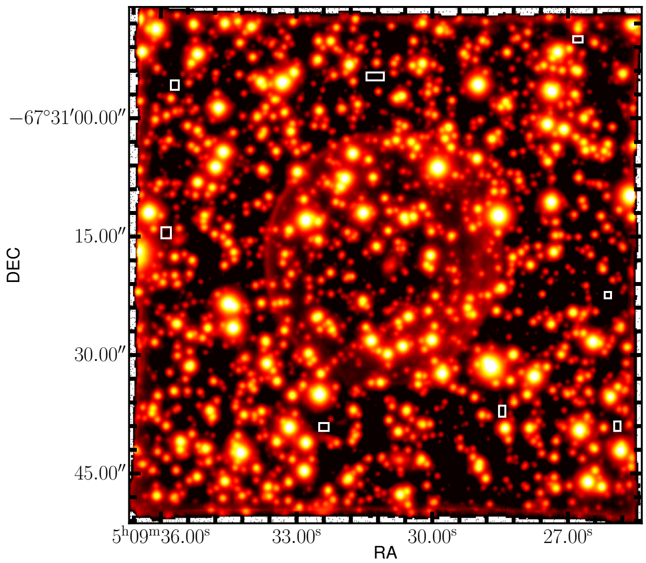

Extended Data Figure. 3 White rectangular boxes represent the area of the sky selected for additional background subtraction. This additional step reduces the contamination by sky emissions significantly

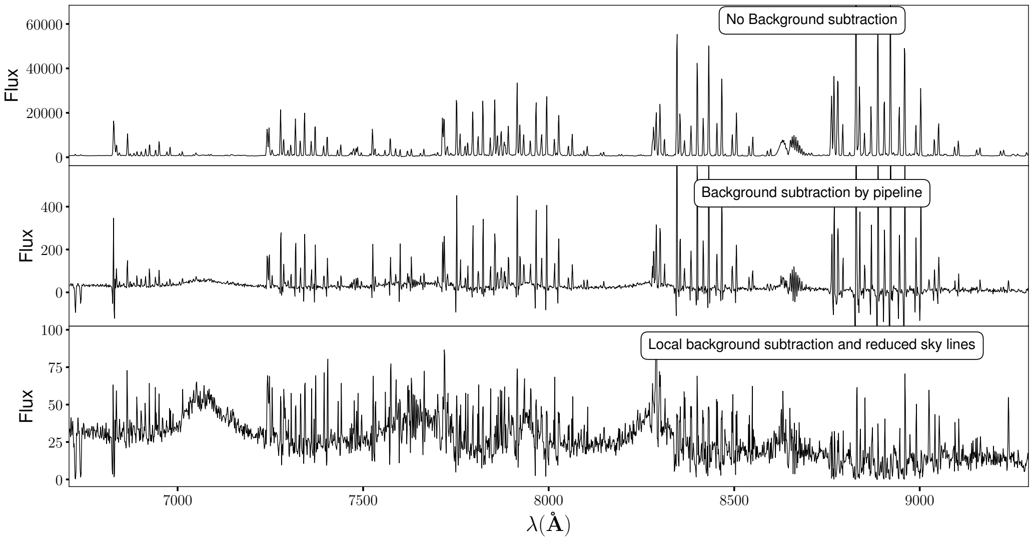

Extended Data Figure. 4 Changes in the spectrum with different stages of data reduction by background sky subtraction and removal of sky-lines